International Journal of Research
Available at https://edupediapublications.org/journals
p-ISSN: 2348-6848
e-ISSN: 2348-795X
Volume 03 Issue 14
October 2016

FLYBACK MODE FOR IMPROVED LOW POWER EFFICIENCY IN THE DUAL ACTIVE BRIDGE CONVERTER FOR BI DIRECTIONAL

RAVI REMIDALA[1], S. MADHANIKA[2]

[1]Assistant Professor, Laqshya institute of tech. & sciences, Khammam

[2]PG Scholar, Laqshya institute of tech. & sciences, Khammam

***Abstract*—This paper targets photovoltaic microinverters (MIVs) with integrated battery storage. The dual-active-bridge (DAB) topology provides bidirectional power flow; however, it generally suffers from poor efficiency and limited regulation accuracy at low power. It is shown that by modifying one switch, the DAB converter can operate as a two-transistor flyback to resolve these two issues. In addition, the dc-link voltage in the two-stage MIV can be dynamically adjusted for optimal performance in DAB mode. The proposed dual-mode control scheme is demonstrated experimentally on a 100-W prototype, with up to 8% increase in converter efficiency at lowpower.**

***Index Terms*—Dual active bridge (DAB), isolated dc–dc converter, photovoltaic (PV) microinverters (MIVs).**

I. INTRODUCTION

THE global population without access to electricity exceeds 1.4 billion, whereas the rural electrification rate is below 65% [1]. An estimated 171 TWh of off-grid electricity will need to be generated by 2030, which is equivalent to 100 GWp of pho- to photo voltaics (PVs) [1]. The intermittent nature of PV and other renewable energy sources, and thus the need for energy storage and/or load shedding, is a major challenge in small-scale PV-based power grids. This is despite power quality requirements. Low-power dc–dc microconverters [2], [3] and ac–dc microinverters (MIV) [4], [5] provide high-granularity maxi- mum power point tracking (MPPT) [6], [7] at the module or substring level. This leads to increased robustness to clouds, dirt, and aging effects, as well as irradiance and temperature gradients [7]. A conventional MIV-based ac power system is shown in Fig. 1. The energy storage system (ESS), which is definitely required for islanded operation on the scale of one or more houses, for example, is usually based on a high-power centralized bidirectional ac–dc converter, which is interfaced to a battery bank or a flywheel [8], [9].

Existing MIV architectures satisfy the need for low capital cost and expandable ac generation, whereas there is a com- pelling argument to extend this technology to include small- scale distributed storage. A novel topology with distributed storage is proposed in [10] for grid stabilization while poten- tially improving the generator lifetime and saving fuel.

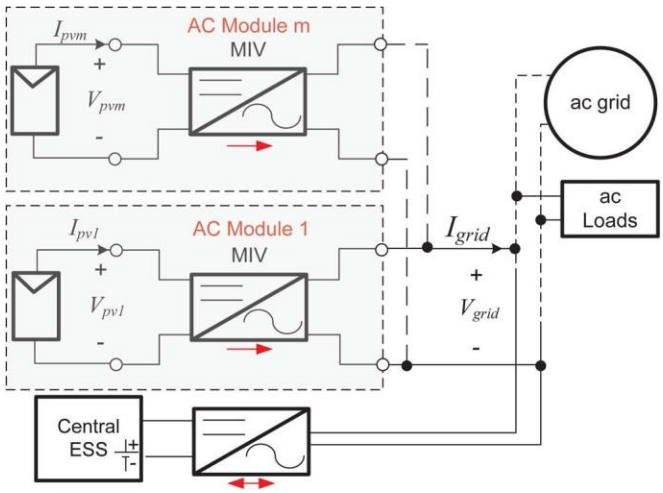

Fig. 1. Conventional MIV-based PV system with a central ESS.

MIV integrated storage helps to buffer the frequent irradiance fluc- tuations while also providing local backup power and reactive power support [11], [12]. A low-power single-stage multiport converter for PV and battery is proposed in [13], whereas a 3-kW interconnection of a battery pack and a PV module through an isolated dc–dc converter is discussed in [14]. The general architecture of a two-stage MIV with an integrated ESS is shown in Fig. 2. While two-stage MIVs have a slightly lower efficiency than their single-stage counterparts, the high-voltage dc-link capacitance C_{bus} can be used for ac power decoupling in single-phase systems [15], [16].

Interfacing the low-voltage dc storage, either batteries or ultracapacitors, directly to the PV bus is preferable for high efficiency [14]. Lithium-ion ultracapacitors [17], which offer 2–4× higher specific energy than conventional electric double-layer capacitors and can withstand more than 200 000 charge/discharge cycles, are an attractive future candidate for short-term MIV integrated storage. The focus of this paper is on the front-end dc–dc stage.

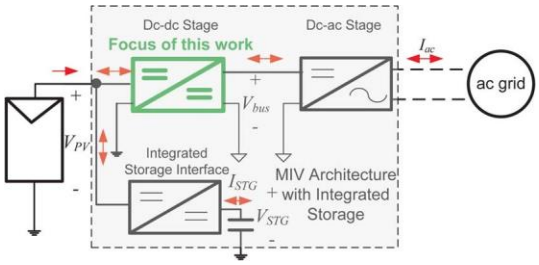

Fig. 2. Two-stage MIV architecture with integrated storage [10].

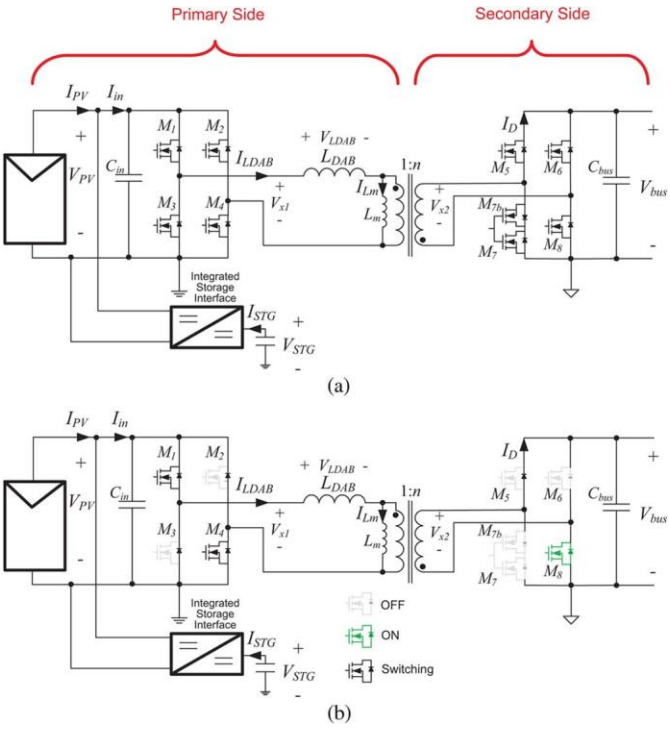

Fig. 3. (a) Proposed modified DAB dc–dc architecture for improved low-power efficiency. (b) Switch configuration in flyback mode.

The objective of this paper is to demonstrate a novel low-power operating mode in the dual-active-bridge (DAB) converter, as well as a dynamic dc-link optimization scheme to maintain high efficiency over a broad power range. This is crucial in any commercial MIV architecture; for example, the European efficiency index dedicates 32% of the total evaluation weight to operation below 30% of the rated power [18]. This paper is an extension of [19] and includes an analysis of the quantization effects, regulation accuracy, and magnetics-related issues in both operating modes.

This paper is organized as follows. The dual-mode converter operation is described in Section II, and relevant quantization issues are discussed in Section III. Magnetics design and converter loss analysis are provided in Sections IV and V, respectively, whereas the simulation and measurements for the experimental prototype are reported in Section VI.

II. Proposed DAB Architecture and Principle of Operation

The proposed dc–dc architecture is shown in Fig. 3(a). This converter is a modified DAB that interfaces V_{PV} with the dc link V_{bus}.

A. DAB Mode

The DAB topology was selected based on 1) galvanic isolation, 2) soft-switching operation, and 3) simple phase-shift power control [20], [21]. In addition, the DAB topology is bidirectional; therefore, the storage can be used to transfer energy to/from other elements in the grid. The average power from V_{PV} to V_{bus}, i.e., P, is

$$P = \frac{V_{PV} V_{bus}}{n\omega_s L_{DAB}} \varphi \left(1 - \frac{|\varphi|}{\pi}\right) \quad (1)$$

where n is the transformer's turns ratio; and L_{DAB} is the DAB inductance, which is the sum of transformer's leakage inductance L_{leak} and an optional external inductance L_{ext}. φ is the phase shift between the two bridges, and $\omega_s = 2\pi f_s$, where f_s is the switching frequency.

The switching waveforms of the DAB converter are shown in Fig. 4(a). The slopes of the DAB inductance current I_{LDAB} in switching states I and II are, respectively, calculated as

$$s_1 = \frac{V_{PV} + \frac{V_{bus}}{n}}{L_{DAB}} \quad (2)$$

$$s_2 = \frac{V_{PV} - \frac{V_{bus}}{n}}{L_{DAB}}. \quad (3)$$

In two-stage MIV architectures, V_{bus} is generally regulated to a fixed voltage by the inverter stage. The reference voltage V_{bus}^* is usually chosen to optimize efficiency at the nominal operating point [7]. It can be shown that the DAB converter achieves turn-on zero-voltage switching (ZVS) and maximum efficiency when $V_{bus} = nV_{PV}$, as the reactive circulating current is minimized [20]. Meeting this condition leads to $s_2 = 0$, thereby resulting in full free-wheeling in I_{LDAB} during state II.

In order to minimize the losses in the DAB, the reference for the dc-link voltage V_{bus}^* is dynamically adjusted in the inverter stage such that $V_{bus}^* = nV_{MPP}$, where V_{MPP} is the PV MPP voltage. It is well known that V_{MPP} undergoes a relatively low fluctuation of about 30% during the course of a typical day [22]. This is in contrast to the PV current at MPP, i.e., I_{MPP}, which is proportional to irradiance and thus has large-scale fluctuations, particularly on cloudy days.

B. Flyback Mode

A typical PV generator spends more than two thirds of the time operating below 50% of its rated power [7]. The conventional DAB converter suffers from relatively poor efficiency at low power due to high switching and drive losses [20], hence the need for a dedicated low-power mode. A general design method for DAB mode operation based on frequency optimization is introduced in [20]. Burst-mode operation in DAB mode has been recently proposed in [23] and [24]. By driving M_1 and M_4 simultaneously on the primary side, the converter can be operated similar to a conventional two-transistor flyback converter (2T-flyback) [25]. The switch configuration in flyback mode is shown in Fig. 3(b). The switches M_1 and M_4 remain active, M_8 is kept *on*, and all other switches are *off*. The secondary-side bridge is modified by adding one switch, i.e.,

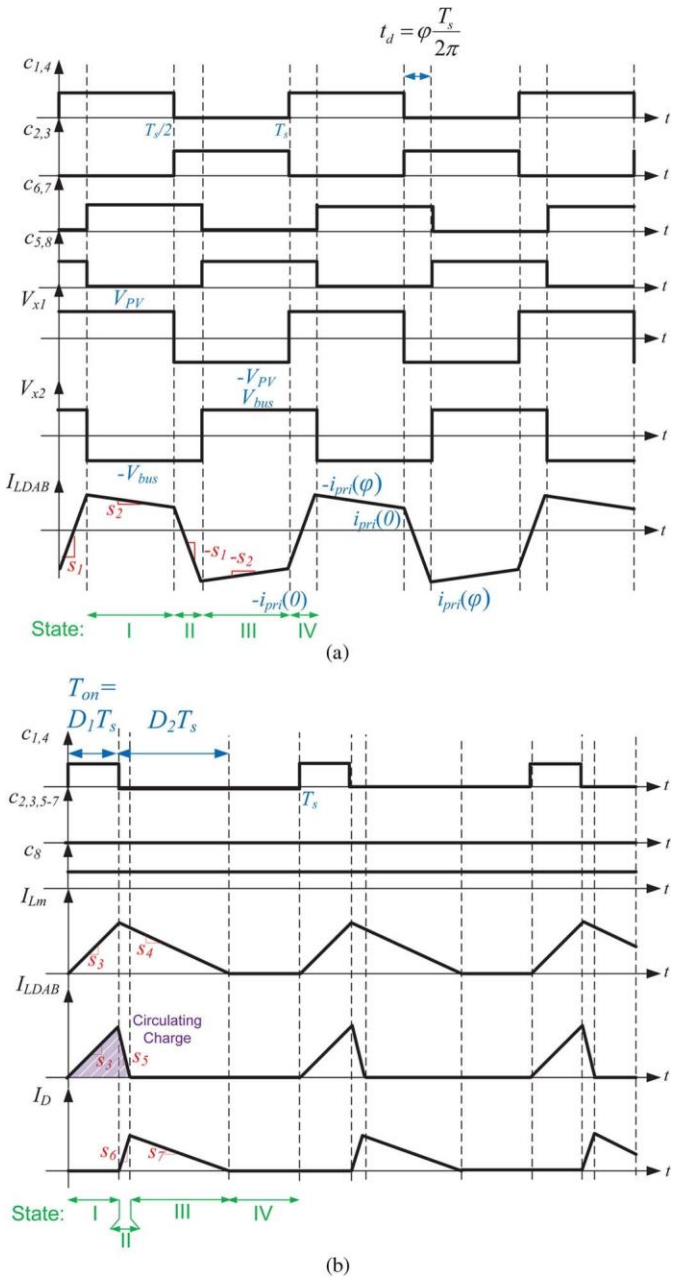

Fig. 4. Switching waveforms in (a) DAB mode and (b) flyback mode.

M_{7b}, to achieve bidirectional blocking capability in flyback mode. The rising and falling slopes of the magnetizing inductance current, i.e., I_{Lm}, are given by

$$s_3 = \frac{V_{PV}}{L_{DAB} + L_m} \quad (4)$$

$$s_4 = \frac{-V_{bus}}{nL_m}. \quad (5)$$

The DAB inductance circulates energy in every switching period in this mode. The rising slope of I_{LDAB} is the same as s_3, and the falling slope is

$$s_5 = \frac{-V_{PV} - \frac{V_{bus}}{n}}{L_{DAB}}. \quad (6)$$

Finally, the output diode current I_D delivers charge to the bus with the following slopes in switching states II and III:

$$s_6 = \frac{s_4 - s_5}{n} \quad (7)$$

$$s_7 = \frac{s_4}{n}. \quad (8)$$

The 2T-flyback topology exhibits several advantages over DAB mode for low-power conditions, including lower switching and gate-driver losses (two switching devices versus nine in the DAB mode). Unlike the more conventional single-transistor flyback topology, the body diodes of M_2 and M_3 clamp the drain voltage on M_1 and M_4, which reduces electromagnetic interference and limits the blocking voltage rating on the primary switches to V_{PV}. The flyback mode is operated with fixed on-time, i.e., T_{on}, in pulse frequency modulation mode [26], where T_{on} is given by

$$T_{on} = D_1 T_s \quad (9)$$

where D_1 is the duty cycle in flyback mode, and T_s is the switching period.

The corresponding converter waveforms are shown in Fig. 4(b). There are two inherent limitations to the 2T-flyback topology: 1) D_1 must be less than 50% in order to avoid transformer saturation; and 2) V_{bus} must be less than nV_{PV} to ensure that the body diode of M_5 transfers power to V_{bus} when the primary-side switches are *off*. As a result, V_{bus} needs to be reduced in flyback mode. The presence of L_{DAB}, which is not required in the 2T-flyback topology, results in additional losses, since it circulates current in a switching period. The energy captured in L_{DAB} is transferred back to the input capacitance C_{in} in the 2T-flyback topology, as opposed to a conventional flyback scheme, which does not provide a return path for the energy absorbed by the leakage inductance. In addition, L_{DAB} results in the soft turn-on of the output diode.

The flyback mode exhibits unidirectional power transfer. The converter can operate with reverse power flow by adding another switch on the primary side. This additional switch is not included in the experimental prototype, as the efficiency in DAB mode is sensitive to conduction losses at the low-voltage high-current primary side. While possible, reverse power capability is not strictly needed in low-power flyback mode; the DAB can be prevented from operating in this condition by adopting burst-mode control instead, albeit at slightly lower efficiency than flyback mode.

C. Dual-Mode Control

The conceptual control diagram of the converter is shown in Fig. 5. c_{1_8} denote the gating voltages for switches M_{1_8}. The DAB mode is adopted if P is higher than a threshold value P_{thresh} or if P is negative, in which case the storage is charged directly from the bus. In DAB mode, φ is controlled to regulate the power flow to/from the dc–ac stage, whereas the storage element's state-of-charge and MPPT operation can be controlled by the dedicated interface converter.

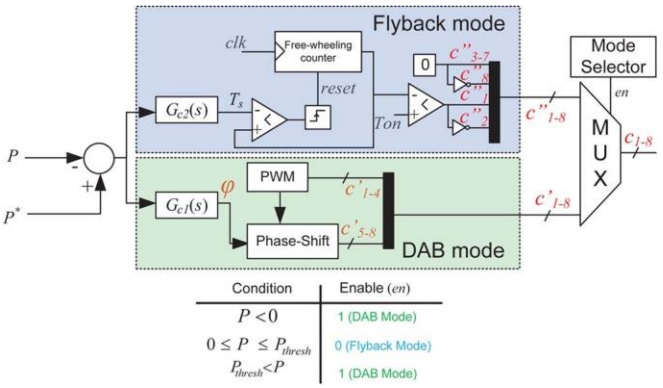

Fig. 5. Simplified conceptual control diagram.

In flyback mode, T_s is adjusted by the controller $tt_{c2}(s)$, in order to regulate P to P^*. Assuming that the magnetizing inductance of the transformer, i.e., L_m, is much larger than L_{DAB}, the power flow is given by

$$P = \frac{(V_{PV} D_1)^2 T_s}{2L_m}. \quad (10)$$

III. Regulation Accuracy at Low Power

As discussed in Section II, the input power of the converter, i.e., P, is regulated in both DAB and flyback modes. However, as the following analysis demonstrates, the power regulation accuracy is greatly improved by operating in flyback mode at low-power levels. In turn, this alleviates the potential for limit-cycle oscillations. Limit-cycle oscillations are commonly observed in digitally controlled switched-mode power supplies based on the quantizer resolutions, whether in current-mode [27] or voltage-mode control [28].

The power versus time shift, t_d of a DAB converter with switching frequency f_s = 195 kHz is shown in Fig. 6(a). The plot includes the theoretical prediction from (1) for an ideal converter, as well as the simulated result for a nonideal converter having the same specifications as the experimental prototype.

The ideal incremental power versus time shift, i.e., dP/dt_d, is also shown in the same figure, which peaks at $P = 0$. Namely,

$$\frac{dP}{dt_d} = -\frac{t_d}{|t_d|}\frac{V_{PV} V_{bus}}{n\omega_s L_{DAB}}\left[\frac{2\pi}{T_s}\left(1 - \frac{4}{T_s}|t_d|\right)\right]. \quad (11)$$

This results in a nonlinear incremental power versus phase-shift profile in the DAB mode, with the regulation accuracy being worse in the low-power region.

In flyback mode, the converter operates with variable switching frequency $f_s = 1/T_s$. The power versus T_s is shown in Fig. 6(b) for both the ideal case based on (10) and simulated converter considering the conduction losses. The ideal dP/dT_s factor in this mode is given by

$$\frac{dP}{dT_s} = -\frac{(V_{PV} T_{on})^2}{2L_m T_s^2}. \quad (12)$$

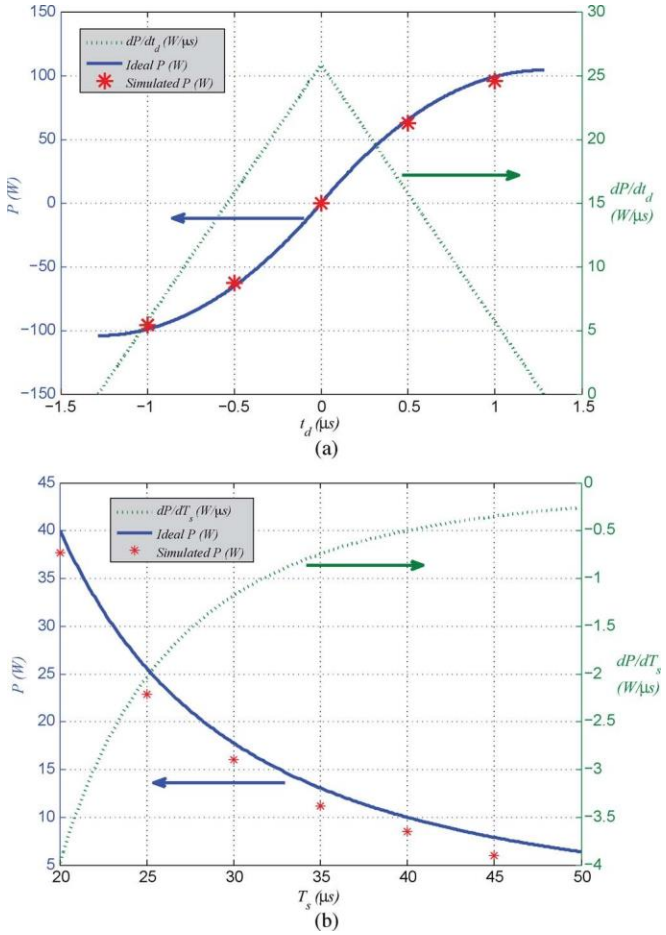

Fig. 6. (a) P and dP/dt_d in DAB mode. (b) P and dP/dT_s in flyback mode.

The incremental power in flyback mode has the opposite trend compared to DAB mode; dP/dT_s is less at low-power levels, which improves the accuracy of the power regulation loop.

Based on a time resolution of 20 ns for the 50-MHz clock used in the prototype, and according to Fig. 6, a single LSB increase in t_d at P = 6 W results in a 50-mW (0.8%) increase in P in flyback mode. However, the same LSB increase in DAB mode results in a 480-mW (8%) increase in P, which corresponds to more than 3 bits of reduction in the effective control resolution. Dual-mode operation therefore benefits not only the efficiency but also the control performance.

IV. Transformer Design

The transformer designed for dual-mode operation is shown in Fig. 7(a). The 3C95 ferrite material has low core losses up to 100 °C [29]. The typical magnetic flux density versus magnetic field for this material is shown in Fig. 7(b). Assuming a gapless core, the transformer in DAB mode exhibits the following peak magnetic flux density which is independent of the power level:

$$B_{peak} = \frac{1}{4A_c n_2} V_{bus,dab} \cdot T_{s,dab} \quad (13)$$

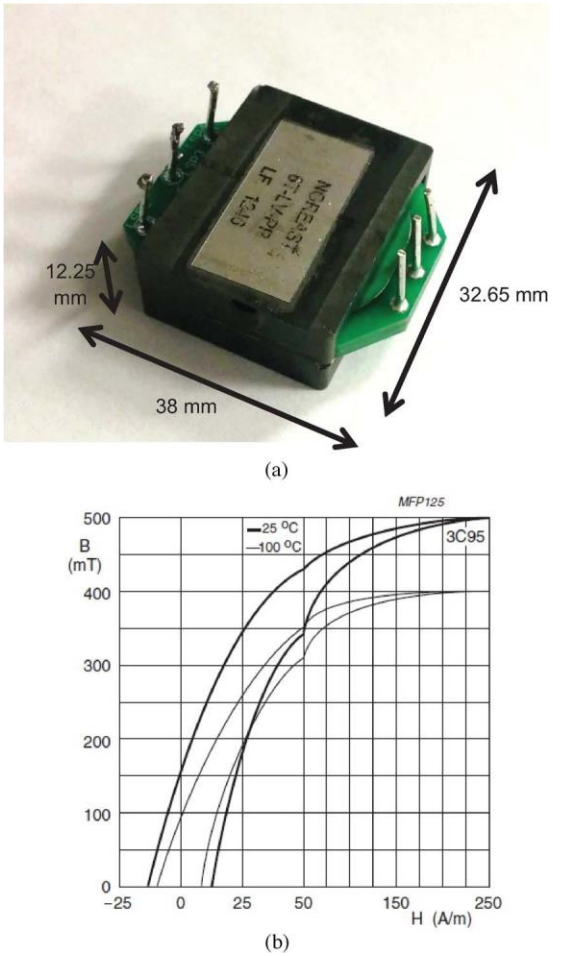

Fig. 7. (a) Planar transformer used in this paper for dual-mode operation. (b) Typical *B-H* curve for C95 magnetic material [29].

where A_c is the core's cross-sectional area, $T_{s,dab}$ is the switching period in DAB mode, $V_{bus,DAB}$ is the dc-link voltage in DAB mode, and n_2 is the number of turns on the secondary winding of the transformer. Assuming that L_{DAB} L_m, B_{peak} in flyback mode depends on T_{on} and is given by

$$B_{peak} = \frac{1}{A_c n_1} V_{PV} \cdot T_{on} \quad (14)$$

where n_1 is the number of turns on the primary winding of the transformer. Comparing (13) and (14), the maximum on-time in flyback mode is limited to

$$T_{on} \leq \frac{1}{4n} \frac{V_{bus,dab}}{V_{PV}} T_{s,dab} \quad (15)$$

such that peak flux density does not exceed the value from DAB mode. For example if $V_{bus,dab} = nV_{PV}$, and $T_{s,dab} = 5.12\ \mu s$, the maximum T_{on} is 1.28 μs. Replacing (15) in (10), and considering the fact that $D_1 \leq 0.5$ and $V_{bus,dab} = nV_{PV}$, the maximum power transfer in flyback mode is therefore given by

$$P_{fl,max} = \frac{V_{PV}^2 T_{s,dab}}{16 L_m}. \quad (16)$$

In practice, the transformer in a DAB converter is designed to limit the core losses at the rated power and maximum frequency, which results in the saturation flux density of the material being well above B_{peak} from (13). In this case, it is possible to increase T_{on} substantially higher than predicted by (15) for the flyback operation at low power and low frequency, without resorting to a gapped core. In this paper, a T_{on} value of 8 μs was used to achieve $P_{thresh} = 40$ W in flyback mode without introducing an air gap into the core. The maximum *on*-time suggested by (15) is 1.28 μs, hence, the core operates with a significantly higher B_{peak} in flyback mode.

V. Efficiency Analysis

This section discusses the dominant power losses in the DAB and flyback modes. An approximate loss analysis is useful to evaluate the threshold reference power value P_{thresh}.

A. Conduction Losses

As shown in Fig. 4(a), the current into the leakage inductance and primary winding of the transformer approach a perfect trapezoid when $V_{bus} = nV_{PV}$. The following equation for the RMS current at the primary side of transformer, i.e. I_{pri}, can be obtained from [21]

$$I_{pri} = \frac{1}{3\pi} \left(i_{pri}(0)^2 \gamma + i_{pri}(\varphi)^2 (\varphi - \gamma) + (\pi - \varphi) \left(i_{pri}(0)^2 + i_{pri}(\varphi)^2 - i_{pri}(0) i_{pri}(\varphi) \right) \right) \quad (17)$$

where

$$\gamma = \frac{i_{pri}(0)}{i_{pri}(0) - i_{pri}(\varphi)} \quad (18)$$

and $i_{pri}(0)$ and $i_{pri}(\varphi)$ are the instantaneous currents of the transformer at the primary side at times $t = 0$ and $t = \frac{\varphi}{\omega_s}$, respectively. These can be easily calculated considering the symmetry of the transformer current [21]

$$i_{pri}(0) = \frac{1}{2L_{DAB}\omega_s} \left(\pi V_{PV} - (\pi - 2\varphi) \frac{V_{bus}}{n} \right) \quad (19)$$

$$i_{pri}(\varphi) = \frac{1}{2L_{DAB}\omega_s} \left((\pi - 2\varphi) V_{PV} - \pi \frac{V_{bus}}{n} \right). \quad (20)$$

Similar calculations can be done for the transformer's secondary-side RMS current, i.e., I_{sec}. Two primary and two secondary switches are conducting at each instance in DAB mode. Thus, the conduction losses in this mode are approximated by

$$P_{DAB,cond} = (2R_{on,pri} + R_{L_{DAB}}) I_{pri}^2 + 2.5 R_{on,sec} I_{sec}^2 \quad (21)$$

where $R_{on,pri}$ and $R_{on,sec}$ are the primary and secondary-side switches' on-resistances, respectively, and $R_{L_{DAB}}$ is the lumped winding resistance of the transformer and inductor. The factor of 2.5 $\times$ on the secondary side comes from the fact that there are two back-to-back switches, namely, M_7 and M_{7b} on one leg in the secondary side to support the flyback operation. All five switches on the secondary side are chosen to be identical.

This results in slightly asymmetrical voltage on transformer taps during one switching cycle in the DAB mode. The on-resistance of the MOSFETs used in the secondary side of the converter has a relatively high positive temperature coefficient. The resulting thermal feedback mechanism helps to avoid transformer saturation or significant dc magnetizing flux in the transformer in DAB mode.

Neglecting the clamping diodes' conduction interval, the RMS current for the two switches, i.e., I_{M_1,M_4}, and in the out- put diode, i.e., D, in the 2T-flyback converter can be obtained as [30]

$$I_{M_1,M_4} = \frac{nP\sqrt{D_1}}{V_{\text{bus}}(1-D_1)} \quad (22)$$

$$I_D = \frac{D_2 T_s V_{\text{bus}}}{n^2 L_m}\sqrt{\frac{D_2}{3}} \quad (23)$$

where D_2 is approximated by

$$D_2 = \frac{nV_{\text{PV}}D_1}{V_{\text{bus}}}. \quad (24)$$

The total conduction loss in flyback mode is

$$P_{\text{Flbk,cond}} = (2R_{\text{on,pri}} + R_{L_{\text{DAB}}})I_{M_1}^2 + V_F I_D + R_{\text{on,sec}} I_D^2 \quad (25)$$

where V_F is the output diode's forward voltage.

B. Switching Losses

The switches in DAB mode can be turned *on* realizing ZVS [21]. However, the turnoff losses are not fully eliminated. Assuming the output capacitance of MOSFETs is small enough, the total switching losses in this mode can be approximated by

$$P_{\text{DAB,sw}} = \frac{1}{2} f_s t_{\text{off}} (V_{\text{PV}}(i_{\text{pri}}(0) + i_{\text{pri}}(\varphi)) + V_{\text{bus}}(i_{\text{sec}}(0) + i_{\text{sec}}(\varphi))) \quad (26)$$

where t_{off} is the turnoff time of the MOSFETs.

Switches M_1 and M_2 exhibit hard switching at turnoff in flyback mode. Thus, the corresponding switching loss in flyback mode can be approximated as

$$P_{\text{Flbk,sw}} = \frac{V_{\text{PV}}^2 D_1 t_{\text{off}}}{2(L_{\text{DAB}} + L_m)}. \quad (27)$$

The gate-driver losses are not analyzed here in detail; however, there are nine active switches in DAB mode compared to only two in flyback mode. Considering that f_s is lower in flyback mode, the overall gate-driver losses are drastically reduced.

C. Core Losses

Core losses are present in the high-frequency transformer and external inductor L_{DAB} in both DAB and flyback modes and can be approximated using the Steinmetz equation [31]

$$P_{\text{core}} = k f_s^{\alpha} B_{\text{peak}}^{\beta} \quad (28)$$

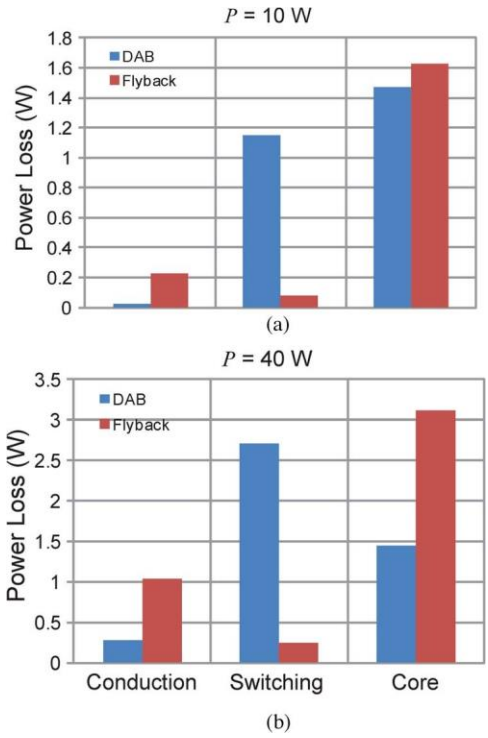

Fig. 8. Simulated power losses for (a) $P = 10$ W and (b) $P = 40$ W.

where B_{peak} is the peak flux density, and k, α, and β are the Steinmetz parameters, which depend on the core material. Core losses constitute a relatively low percentage of the total losses in DAB mode [21] due to high-frequency ac–ac operation. However, core losses are dominant in flyback mode. This simplified analysis neglects the skin effect in all conductors, which can be significant, particularly in DAB mode due to high frequency operation.

A. Loss Comparison in Two Modes

The calculated loss breakdown for $P = 10$ W and $P = 40$ W is shown in Fig. 8. The conduction losses in all active and passive elements are lumped together. The switching losses also include the drive losses. In flyback mode, the switching losses are reduced by at least 10 ×, mostly by eliminating the turnoff losses on the high-voltage side, at a cost of marginal increase in conduction losses. The transformer and inductor core loss is slightly higher in flyback mode, due to higher B_{peak}. The core losses in flyback mode rapidly increase with the power due to higher B_{peak} and f_s. This is not the case for the DAB converter, in which the core losses remain almost constant over the full phase shift range due to constant L_m excitation based on (13) [32].

VI. Simulation and Experimental Results

A prototype of the system shown in Fig. 3(b) was fabricated on a custom printed circuit board, with power rating of 100 W. The main specifications of the prototype are listed in Table I. A minimum frequency of 20 kHz is adopted in flyback mode to avoid interfering with the audible range, whereas a fixed frequency of 195 kHz is adopted for DAB mode, based on

International Journal of Research
Available at https://edupediapublications.org/journals
p-ISSN: 2348-6848
e-ISSN: 2348-795X
Volume 03 Issue 14
October 2016

TABLE I
MIV PROTOTYPE SPECIFICATIONS

Parameter	Value	Units
Rated Power, P_{nom}	100	W
Dc-dc Stage Switching Frequency, f_s		
DAB Mode	195	kHz
Flyback Mode	20-50	kHz
Fixed On-Time, T_{on}	8	μs
Input Capacitance, C_{in}	300	μF
Bus Capacitance, C_{bus}	100	μF
DAB Inductance, L_{DAB}	4.2	μH
Magnetizing Inductance, L_m	32	μH
Bus Voltage Range, V_{bus}		
DAB mode	200-270	V
Flyback mode	170	V
Transformer Turns Ratio, n	9	

optimized efficiency. The DAB converter can be operated with lower frequencies without saturating the magnetic cores; however, reducing the switching frequency increases RMS currents in the converter. Furthermore, the turnoff process happens at higher current values, and thus, the total switching losses do not scale down linearly with frequency. For example, reducing the switching frequency by 50% increases the RMS current in primary, secondary, and active devices by about 38% at $P = 70$ W, which translates into ≈90% more conduction losses, whereas the total switching losses are reduced by 22%.

The converters are digitally controlled using an onboard field-programmable gate array. A custom planar transformer shown in Fig. 7(a) was designed to reduce the weight and profile of the prototype. The suboptimal general operation of the DAB converter without dynamic V_{bus} scaling is shown in Fig. 9(a). The steady-state waveforms in DAB mode with bus voltage scaling ($V_{bus} = nV_{PV}$) and flyback mode at $P = 70$ W and $P = 15$ W are shown in Fig. 9(b) and (c), respectively.

There are two interesting phenomena that are noticeable in flyback mode. First, the oscillations that are observed on the voltage across the DAB inductance, i.e., V_{LDAB}, are due to the resonance of L_{DAB} with output capacitance of MOSFETs on the primary side and the capacitance on the transformer's primary winding. Second, I_{LDAB} has two distinct rising slopes. The rising slope following turn-on is large, then reduces to s_3, as shown in the ideal waveforms in Fig. 4(b). This happens when L_m is not fully demagnetized by the start of the switching cycle in flyback mode. This effect is shown in Fig. 10 when the flyback is operating in continuous conduction mode (CCM). The initial rising slope of I_{LDAB} is equal to s_1 from (2).

Based on Fig. 7(b), L_m significantly increases at low magnetizing currents. This prevents the full demagnetization of L_m in one switching cycle. As a result, I_{Lm} has a minimum value of about 1 A. This effect can be mitigated by introducing an air gap in the transformer. This will reduce the reluctance of the core and linearize L_m for the full operating range.

The closed-loop dynamic response of flyback mode for a step change in P^*, while the dedicated integrated storage converter is off, is shown in Fig. 11. f_s is increased in flyback mode by the controller to accommodate the higher input power.

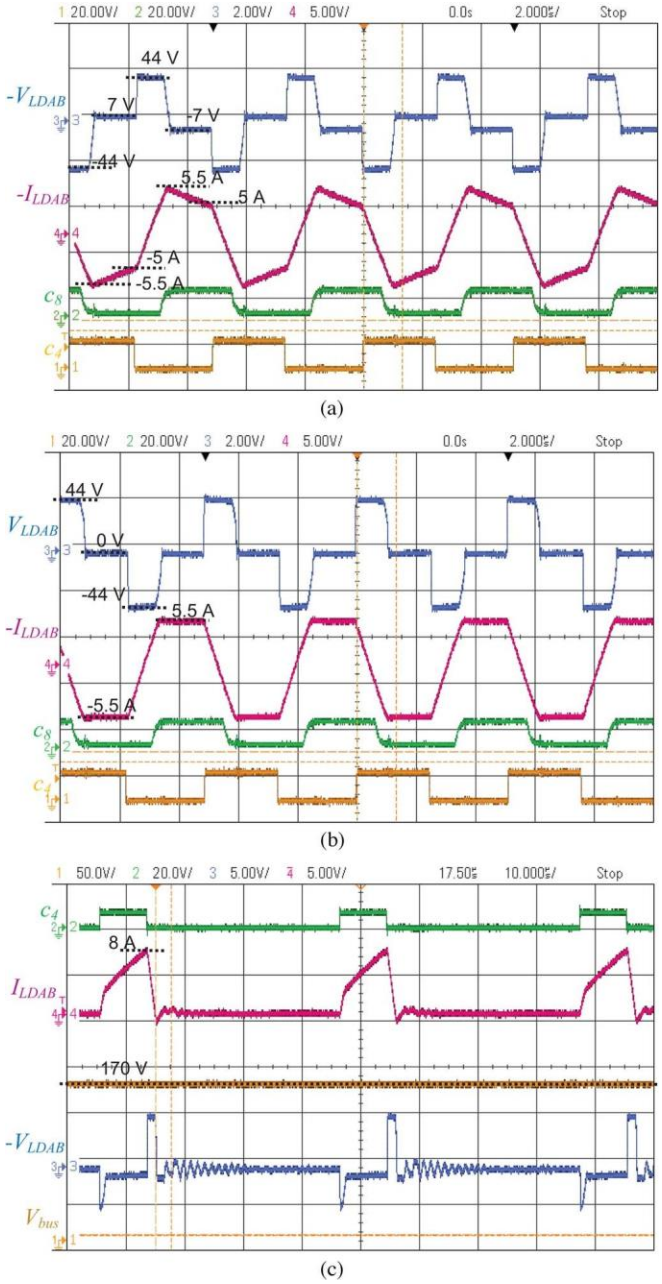

Fig. 9. Steady-state waveforms of the converter in (a) DAB mode without dynamically adjusted dc-link voltage, (b) DAB mode with adjusted dc-link voltage ($V_{bus} = nV_{PV}$) at $V_{PV} = 22$ V (I_{LDAB}: 5 A/div), and (c) flyback mode at $V_{PV} = 25$ V (I_{LDAB}: 5 A/div).

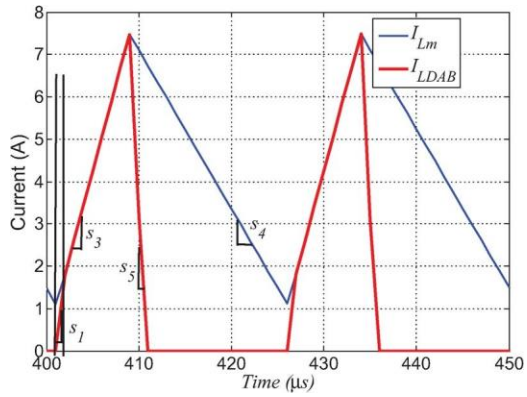

Fig. 10. Simulated I_{LDAB} and I_{Lm} in flyback mode operating in CCM.

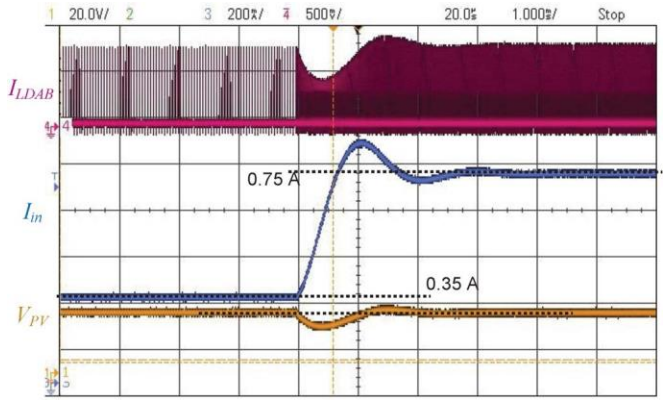

Fig. 11. Measured step response of flyback mode with the integrated storage interface off: P: 9.1 W → 19.5 W (I_{in}: 0.2 A/div, I_{LDAB}: 10 A/div).

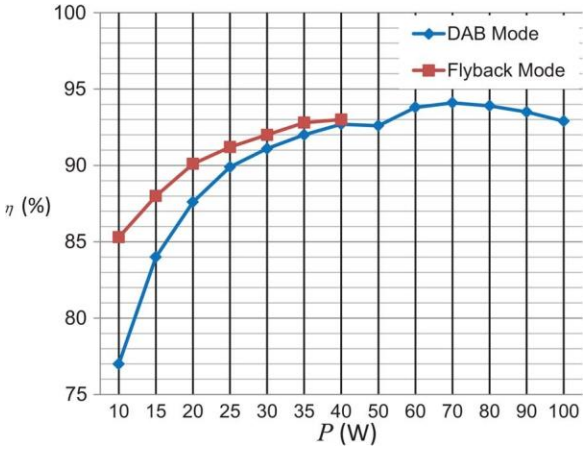

Fig. 12. Measured efficiency η of the converter.

The measured efficiency of the converter, i.e., η, in both modes is shown in Fig. 12. A peak efficiency of 94% is achieved in DAB mode, whereas flyback mode has a superior efficiency up to $P = 40$ W. The power is limited in flyback mode due to the maximum duty ratio of 50%. The design was carried out such that the two efficiency curves intercept at a point close to the maximum transferable power in flyback mode. The operation is switched to DAB mode from flyback mode at this point for higher reference power values.

VII. Conclusion

A novel DAB switching scheme was introduced for the dc–dc stage of module integrated power converters for PV applications. The modified flyback switching scheme exhibits 8% higher efficiency than DAB mode at 10 W, which comes at the cost of an additional switch. While flyback mode exhibits more core losses and slightly more conduction losses compared to DAB mode, the switching losses are significantly reduced by eliminating most of the switching actions and reducing the frequency. In addition, it was shown that the flyback mode achieves higher accuracy in power regulation for low-power levels compared to the DAB mode, resulting in a more stable operation and avoiding potential limit cycle oscillations.

Acknowledgment

The authors would like to thank R. Orr, B. Bacque, M. Varlan, and C. Gerolami for discussions related to nanogrids and microinverters.

References

[1] R. Cabraal, "Experiences and lessons from 15 years of world bank support for photovoltaics for off-grid electrification," in *Proc. 2nd ICDRET*, Jan. 2012, pp. 1–4.
[2] R. K. Hester *et al.*, "High efficiency wide load range buck/boost/bridge photovoltaic microconverter," in *Proc. IEEE Appl. Power Electron. Conf. Expo.*, 2011, pp. 309–313.
[3] B. York, W. Yu, and J.-S. Lai, "An integrated boost resonant converter for photovoltaic applications," *IEEE Trans. Power Electron.*, vol. 28, no. 3, pp. 1199–1207, Mar. 2013.
[4] R. Erickson and A. Rogers, "A microinverter for building-integrated photovoltaics," in *Proc. IEEE Appl. Power Electron. Conf. Expo.*, 2009, pp. 911–917.
[5] "Enphase m190 microninveter," Enphase Datasheet, 2009. [Online]. Available: http://enphaseenergy.com
[6] N. Femia, G. Lisi, G. Petrone, G. Spagnuolo, and M. Vitelli, "Distributed maximum power point tracking of photovoltaic arrays: Novel approach and system analysis," *IEEE Trans. Ind. Electron.*, vol. 55, no. 7, pp. 2610–2621, Jul. 2008.
[7] S. Poshtkouhi, V. Palaniappan, M. Fard, and O. Trescases, "A general approach for quantifying the benefit of distributed power electronics for fine grained MPPT in photovoltaic applications using 3-D modeling," *IEEE Trans. Power Electron.*, vol. 27, no. 11, pp. 4656–4666, Nov. 2012.
[8] L. Xu and D. Chen, "Control and operation of a dc microgrid with variable generation and energy storage," *IEEE Trans. Power Del.*, vol. 26, no. 4, pp. 2513–2522, Oct. 2011.
[9] G. Suvire, M. Molina, and P. Mercado, "Improving the integration of wind power generation into ac microgrids using flywheel energy storage," *IEEE Trans. Smart Grid*, vol. 3, no. 4, pp. 1945–1954, Dec. 2012.
[10] S. Poshtkouhi *et al.*, "A dual-active-bridge based bi-directional microinverter with integrated short-term Li-ion ultra-capacitor storage and active power smoothing for modular PV systems," in *Proc. 29th Annu. IEEE APEC Expo.*, Mar. 2014, pp. 643–649.
[11] M. Alam, K. Muttaqi, and D. Sutanto, "Mitigation of rooftop solar PV impacts and evening peak support by managing available capacity of distributed energy storage systems," *IEEE Trans. Power Syst.*, vol. 28, no. 4, pp. 3874–3884, Nov. 2013.
[12] L. Liu, H. Li, Z. Wu, and Y. Zhou, "A cascaded photovoltaic system integrating segmented energy storages with self-regulating power allocation control and wide range reactive power compensation," *IEEE Trans. Power Electron.*, vol. 26, no. 12, pp. 3545–3559, Dec. 2011.
[13] Y.-M. Chen, A. Huang, and X. Yu, "A high step-up three-port DC–DC converter for stand-alone PV/battery power systems," *IEEE Trans. Power Electron.*, vol. 28, no. 11, pp. 5049–5062, Nov. 2013.
[14] Z. Wang and H. Li, "An integrated three-port bidirectional DC–DC converter for PV application on a DC distribution system," *IEEE Trans. Power Electron.*, vol. 28, no. 10, pp. 4612–4624, Oct. 2013.
[15] H. Hu, S. Harb, N. Kutkut, Z. Shen, and I. Batarseh, "A single-stage microinverter without using eletrolytic capacitors," *IEEE Trans. Power Electron.*, vol. 28, no. 6, pp. 2677–2687, Jun. 2013.
[16] S. Kjaer, J. Pedersen, and F. Blaabjerg, "A review of single-phase grid-connected inverters for photovoltaic modules," *IEEE Trans. Ind. Appl.*, vol. 41, no. 5, pp. 1292–1306, Sep./Oct. 2005.
[17] Lithium-Ion Capacitor, JSR Micro, Sunnyvale, CA, USA, 2012. [Online]. Available: http://www.jsrmicro.com/index.php/EnergyAndEnvironment/
[18] European or CEC Efficiency, PVsyst Photovoltaic, 2015. [Online]. Available: http://files.pvsyst.com/help/
[19] S. Poshtkouhi and O. Trescases, "A dual active bridge DC–DC converter with optimal DC-link voltage scaling and flyback mode for enhanced low-power operation in hybrid PV/storage systems," in *Proc. IPEC-Hiroshima ECCE-ASIA*, May 2014, pp. 2336–2342.
[20] F. Krismer and J. Kolar, "Efficiency-optimized high-current dual active bridge converter for automotive applications," *IEEE Trans. Ind. Electron.*, vol. 59, no. 7, pp. 2745–2760, Jul. 2012.
[21] H. Qin and J. Kimball, "Generalized average modeling of dual active bridge DC–DC converter," *IEEE Trans. Power Electron.*, vol. 27, no. 4, pp. 2078–2084, Apr. 2012.

[22] M. Park and I.-K. Yu, "A study on the optimal voltage for MPPT obtained by surface temperature of solar cell," in *Proc. 30th Annu. Conf. IEEE Ind. Electron. Soc.*, 2004, vol. 3, pp. 2040–2045.
[23] G. Oggier and M. Ordonez, "High efficiency switching sequence and enhanced dynamic regulation for DAB converters in solid-state transformers," in *Proc. IEEE APEC Expo.*, Mar. 2014, pp. 326–333.
[24] A. Rodriguez, A. Vazquez, D. Lamar, M. Hernando, and J. Sebastian, "Different purpose design strategies and techniques to improve the performance of a dual active bridge with phase-shift control," *IEEE Trans. Power Electron.*, vol. 30, no. 2, pp. 790–804, Feb. 2015.
[25] D. D. C. Lu, H.-C. Iu, and V. Pjevalica, "A single-stage AC/DC converter with high power factor, regulated bus voltage, and output voltage," *IEEE Trans. Power Electron.*, vol. 23, no. 1, pp. 218–228, Jan. 2008.
[26] R. Erickson and D. Maksimović, *Fundamentals of Power Electronics*, 2nd ed. Berlin, Germany: Springer-Verlag, 2001.
[27] O. Trescases, A. Prodic, and W.T. Ng, "Digitally controlled current-mode dc–dc converter IC," *IEEE Trans. Circuits Syst. I, Reg. Papers*, vol. 58, no. 1, pp. 219–231, Jan. 2011.
[28] S. Saggini, W. Stefanutti, D. Trevisan, P. Mattavelli, and G. Garcea, "Prediction of limit-cycles oscillations in digitally controlled dc–dc converters using statistical approach," in *Proc. 31st Annu. IEEE IECON*, Nov. 2005, pp. 1–6.
[29] Ferroxcube E65/32/27 Datasheet, Ferroxcube, Taipei, Taiwan, 2004. [Online]. Available: http://www.ferroxcube.com/FerroxcubeCorporateReception/datasheet/e653227.pdf
[30] D. Murthy-Bellur and M. Kazimierczuk, "Two-switch flyback-forward PWM DC–DC converter with reduced switch voltage stress," in *Proc. IEEE ISCAS*, May 2010, pp. 3705–3708.
[31] J. Reinert, A. Brockmeyer, and R. De Doncker, "Calculation of losses in ferro- and ferrimagnetic materials based on the modified Steinmetz equation," *IEEE Trans. Ind. Appl.*, vol. 37, no. 4, pp. 1055–1061, Jul./Aug. 2001.
[32] B. Cougo and J. Kolar, "Integration of leakage inductance in tape wound core transformers for dual active bridge converters," in *Proc. 7th Int. Conf. CIPS*, Mar. 2012, pp. 1–6.

Mr. RAVI REMIDALA was born in India in the year of 1987.He received B.Tech degree in Electrical and Electronics Engineering in the year of 2008 & M.Tech PG in Electrical power systems in the year of 2013 from JNTUH, Hyderabad. He is expert in ControlSystems, Electrical circuits, Power system and electrical machines Subjects. He is currently working as An Associate Professor in EEE Department in Laqshya Institute of Technology and Sciences, Khammam,Telangana State ,India.
mail id: ravi.july25@ gmail.com

SAGGURTHI MADHANIKA **(POWER ELECTRONICS) PURSUING** In **laqshya Institute of Technology sciences ,TALIKELLA(V)** ,KHAMMAM, TELANGANA, INDIA
MAIL: madhanika13@gmail.com